





## Deformations related to atom mixing in Si/SiO<sub>2</sub>/Si nanopillars under high-fluence broad-beam irradiation

C. Fridlund <sup>\*</sup>, A. Lopez-Cazalilla , and K. Nordlund 

*Department of Physics, University of Helsinki, P. O. Box 43, Helsinki FIN-00014, Finland*

F. Djurabekova 

*Helsinki Institute of Physics and Department of Physics, University of Helsinki, P. O. Box 43, Helsinki FIN-00014, Finland*



(Received 20 May 2020; accepted 23 June 2021; published 16 August 2021)

Structures consisting of a single Si nanodot buried within an insulating nanometric SiO<sub>2</sub> layer stacked between two Si layers show promising properties for room temperature operational single-electron transistors. Moreover, such structures are highly compatible with modern *complementary metal-oxide semiconductor* technologies. Metastable SiO<sub>x</sub> phase separates into a Si nanodot and insulating, homogeneous SiO<sub>2</sub> during annealing, providing a solid path towards the desired structure. However, achieving the necessary amount of excessive Si, dissolved in the SiO<sub>2</sub> for correct concentrations of SiO<sub>x</sub>, remains a technological challenge. In this work, we investigate ion-induced atom mixing in pre-built Si/SiO<sub>2</sub>/Si nanopillars, which is considered to be a technologically promising way to produce the necessary concentrations of spatially confined SiO<sub>x</sub> in a controlled manner. During the high-fluence ion irradiation, we notice a significant shortening of the nanopillar and preferential loss of O atoms. Both sputtering and nanoscale ion hammering are found to be the cause of the deformation. The ion-hammering effect on nanoscale is explained by multiple small displacements, strongly enhanced after the nanopillar was rendered completely amorphous. The methods presented here can be used to determine the ion-fluence threshold for sufficient atom mixing in spatially confined regions before the large structural deformations are formed.

DOI: [10.1103/PhysRevMaterials.5.083606](https://doi.org/10.1103/PhysRevMaterials.5.083606)

### I. INTRODUCTION

The power consumption of the increasing number of devices connecting to the Internet-of-Things (IoT), combined with a general stagnation of the power-storage development demand alternative power-saving solutions. By solutions that maintain compatibility with existing production methods while advancing the available components, it is possible to save power without the need to change the entire production pipelines. Single-electron transistors (SETs) have been among the most attractive research fields in microelectronics over the last couple of decades [1]. By integrating these electrical devices with the available semiconductor circuitry, the power consumption of modern devices could decrease notably. Semiconductor-based SET prototypes working at room temperature (RT) have already been demonstrated [2–5], however, there are no reports in the literature showing reliable ways of manufacturing complementary metal oxide semiconductor (CMOS)-compatible SETs commercially at large scales, while maintaining stability at RT.

A general SET consists of three electrodes separated by a dielectric. Within the insulating dielectric a small conductive quantum nanodot (QD) connects the source and the drain through tunnel junctions. The QD functions as an intermediate landing site for electrons tunneling from the source to the

drain. The number of electrons tunneling simultaneously is controlled by the Coulomb blockade [6,7], which raises the energy level of the QD, effectively blocking other electrons from entering while it is already occupied by another electron. The tunneling distance, QD size, and lateral placement of the QD are all crucial for the Coulomb blockade to control the single-electron transport reliably. The strength of the repulsive force exercised by the Coulomb blockade can be altered by varying a small bias voltage coupled capacitively over the gate [6]. This allows the transistor to work on extremely low currents (two to three orders of magnitude lower than current transistors [8]), while still operating like a traditional metal-oxide-semiconductor field-effect transistor (MOSFET) [9]. The size of the QD has to be below 10 nm to express the quantum physical properties needed for stable operation at RT [10].

Experiments show that metastable SiO<sub>x</sub> inside SiO<sub>2</sub> phase separates into stable Si nanoclusters under controlled annealing [11–19]. These nanoclusters behave as QDs of SETs when they are placed optimally within the dielectric layer [10]. One possible solution to create the desired metastable SiO<sub>x</sub> concentration at the right depth, yet confined within a nanosized volume to ensure formation of a single QD, is to irradiate predesigned heterostructural Si/SiO<sub>2</sub>/Si nanopillars [20] with high-fluence broad-beam Si<sup>+</sup> irradiation at normal incidence. The annealing of such a structure activates diffusion processes and a single QD appears close to the lateral center of the SiO<sub>2</sub> layer, driven by a self-assembly process through Ostwald

<sup>\*</sup>Corresponding author: [christoffer.fridlund@helsinki.fi](mailto:christoffer.fridlund@helsinki.fi)

ripening [21,22]. The vertical positioning of a QD can be controlled via the intensity of atomic mixing at the interfaces, i.e., the depth where the concentration of excessive Si atoms with respect to stoichiometric SiO<sub>2</sub> is still significant [17]. Recent experimental advances show a promising way of producing the nanosized pillars [23] ready to be exposed to the high-fluence ion irradiation.

In this work, we use molecular dynamics (MD) to simulate the atomic mixing effects within the heterostructured nanopillar and analyze the dynamics related to the formation of the metastable SiO<sub>x</sub> phase inside the SiO<sub>2</sub> layer as a function of ion fluence. The SiO<sub>x</sub> is formed from excessive Si atoms, introduced from the surrounding Si layers into the SiO<sub>2</sub> matrix during the irradiation. The choice of a pillar as object for the irradiation is motivated by the necessity of lateral confinement of the atomic mixing to force the formation of one single QD per transistor. Irradiation of continuous interfaces, even if they were placed at the correct depth, would result in a two-dimensional (2D) range of QDs [12]. Separating these into single transistors introduces additional technological challenges.

The pillar dimensions and irradiation energies are chosen in compliance with experimental ranges [16,23–25] and the results will be used for comparison with other computational methods and as parametrization of experimental setups. To validate the atom mixing we analyze the density profiles along the depth axis (*z*-axis) and the mechanisms behind the shape changes of the nanopillar with increasing fluence. We verify the density profiles with coordination analysis of the amorphous structures.

## II. METHODS

### A. Simulation setup

All MD simulations were carried out with the PARCAS molecular dynamics code [26,27], using the Stillinger-Weber-like Watanabe-Samela potential [28–30] describing the interatomic interactions between Si–Si, Si–O, and O–O atoms. Electronic stopping was taken into account as a frictional force obtained from the SRIM database [31]. Due to the open surfaces in all directions, no periodic boundary conditions (PBC) nor barostat were used during any of the simulations.

### B. System preparation

For the current study we prepared two different nanopillar structures. The first nanopillar was constructed according to the design measures of a planned SET device [25] (diameter 10 nm and height 51 nm). This pillar had a sandwich-like structure with a 7-nm-thick amorphous silicon dioxide (*a*-SiO<sub>2</sub>) layer buried between a 25-nm (top) and a 19-nm (bottom) thick crystalline silicon (*c*-Si) layer as shown in Fig. 1(a).

To create the sandwich structure, we merged *c*-Si and *a*-SiO<sub>2</sub> layers as described in Ref. [32] and relaxed the stacked system for 600 ps. After that, a cylinder of the required size with a 1-nm-thick rectangular pedestal at the bottom, to account for the substrate where the nanopillar is attached, was cut out from the stacked structure. The pedestal was used

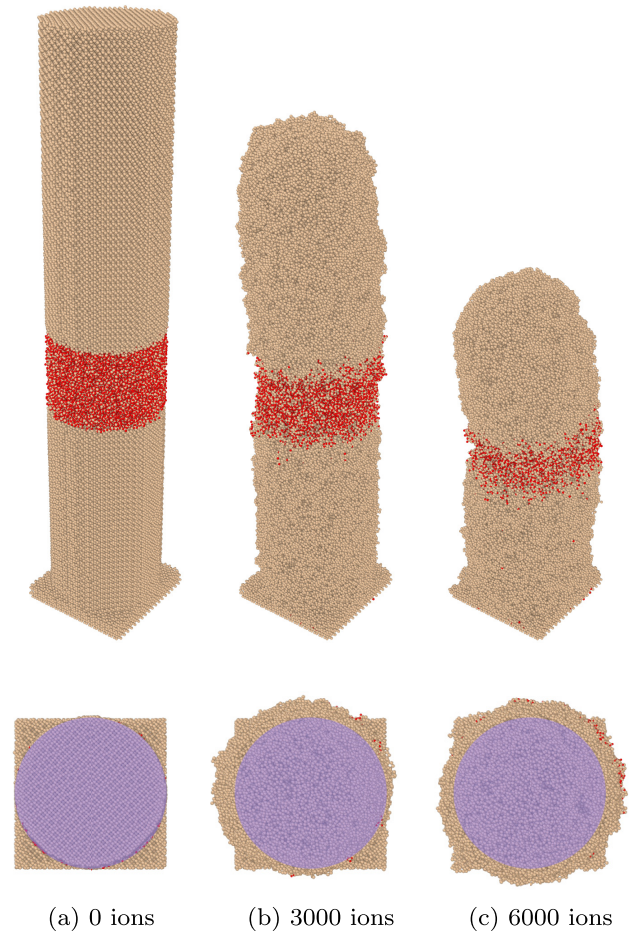


FIG. 1. The deformation of the Si/SiO<sub>2</sub>/Si pillar ( $r = 5$  nm,  $h = 50$  nm) during the irradiation. Here we show the visual damage done to the pillar at three different stages of the irradiation: (a)  $0$  cm<sup>-2</sup>, (b)  $3.8 \times 10^{15}$  cm<sup>-2</sup>, and (c)  $7.6 \times 10^{15}$  cm<sup>-2</sup>. The bottom row of figures shows the projected area exposed to the broad beam. Most of the damage comes from sputtering and the hammering caused by the ions.

for temperature control during the high-fluence irradiation simulation.

We performed an additional annealing run for 100 ps to optimize the surface energy of the pillar. The system was heated to 1200 K at 0.1 K/fs and cooled slowly back down to 300 K at 0.01 K/fs. After this procedure the pillar relaxation was continued with a regular Berendsen thermostat [33] on all atoms in the system for 100 ps. Some atoms detached from the surface during the heating. They were found after the relaxation run using the cluster analysis modifier available in OVITO [34] with  $r_{\text{cutoff}} = 3$  Å, and subsequently removed from the simulation cell.

To analyze the effects of the radiation-enhanced dynamics at the surface we needed a more efficient simulation system and prepared a second, smaller nanopillar out of pure *c*-Si (diameter 7 nm, height 12.5 nm) with a broader (19.5 nm) pedestal. This pillar was prepared following the same recipe as the original one, excluding the step of stacking the different layers together.

Henceforth, we will refer to the original (stacked) structure as the “tall” and the second, smaller one as the “short” nanopillar.

### C. High-fluence ion irradiation of the nanopillars

The high-fluence ion irradiation was simulated as a series of 6000 consecutive ion impacts on the tall nanopillar described in Sec. II B. To simulate a large number of cascades within a reasonable computational time, we applied the same speedup procedure as described in Ref. [32]: ten ion impacts simulated only for 1.0 ps each followed by a 5.0 ps long relaxation with the Berendsen thermostat applied to all atoms. During the active phase of cascade development, the thermostat was applied only to the atoms in the pedestal. At the end of these runs, for the last 0.4 ps, the temperature was rapidly quenched to 300 K everywhere in the cell.

To prevent the systems from gaining a downward momentum from the energetic ion impacts, the bottom-most 0.6 nm (the lowest four to five atomic layers of the pedestal) were fixed throughout the simulation. The ions reaching the fixed region were removed from the simulation cell to avoid possible artifacts caused by the applied boundary conditions (e.g., ion reflections from the fixed layers, etc.).

We targeted the tall pillar with broad-beam 25 keV Si<sup>+</sup> ion irradiation at normal incidence and initiated  $\sim 1$  nm above the initial height of the nanopillar tip. The lateral coordinates of the ions were randomly chosen within the circular area of the apex of the nanopillar shown in Fig. 1. All sputtered atoms were removed before the next ion impact.

The irradiation of the short nanopillar was initiated in the same way as for the tall nanopillar, but using 11 keV Si<sup>+</sup> ions. It was set up in a full broad-beam regime, i.e., the lateral extents of the pedestal was used to randomize the starting position of the ions. By applying PBC in the lateral directions, we allowed redeposition of sputtered atoms over the periodic boundaries. The ion energy was estimated from SRIM2013 [31] to ensure that the range of the maximum energy deposition (7 nm to 10 nm) coincided with the bottom half of the pillar.

## III. RESULTS AND DISCUSSION

### A. Nanopillar deformations due to high-fluence ion irradiation

The shape evolution of the nanopillar during prolonged ion irradiation can be seen in Fig. 1, where we show the snapshots taken [Fig. 1(a)] before any irradiation, [Fig. 1(b)] after  $3.8 \times 10^{15} \text{ cm}^{-2}$  fluence, and [Fig. 1(c)] after the final fluence of  $7.6 \times 10^{15} \text{ cm}^{-2}$ . Visual inspection of these images revealed the following transformations: (i) the *c*-Si turned into *a*-Si; (ii) the sharp Si/SiO<sub>2</sub> and SiO<sub>2</sub>/Si interfaces became more diffuse; (iii) the overall thickness of the SiO<sub>2</sub> slab, which gradually became SiO<sub>x</sub> due to atom mixing, kept decreasing; and finally, (iv) the height of the pillar decreased dramatically over the course of the irradiation. In the following, we focus on (iii) and (iv). Understanding the first is important because of the need to have a sufficient amount of excessive Si in the *a*-SiO<sub>2</sub> layer, and the second because it affects the geometric composition of the pillar, imposing additional demands on the design process of the final SET device.

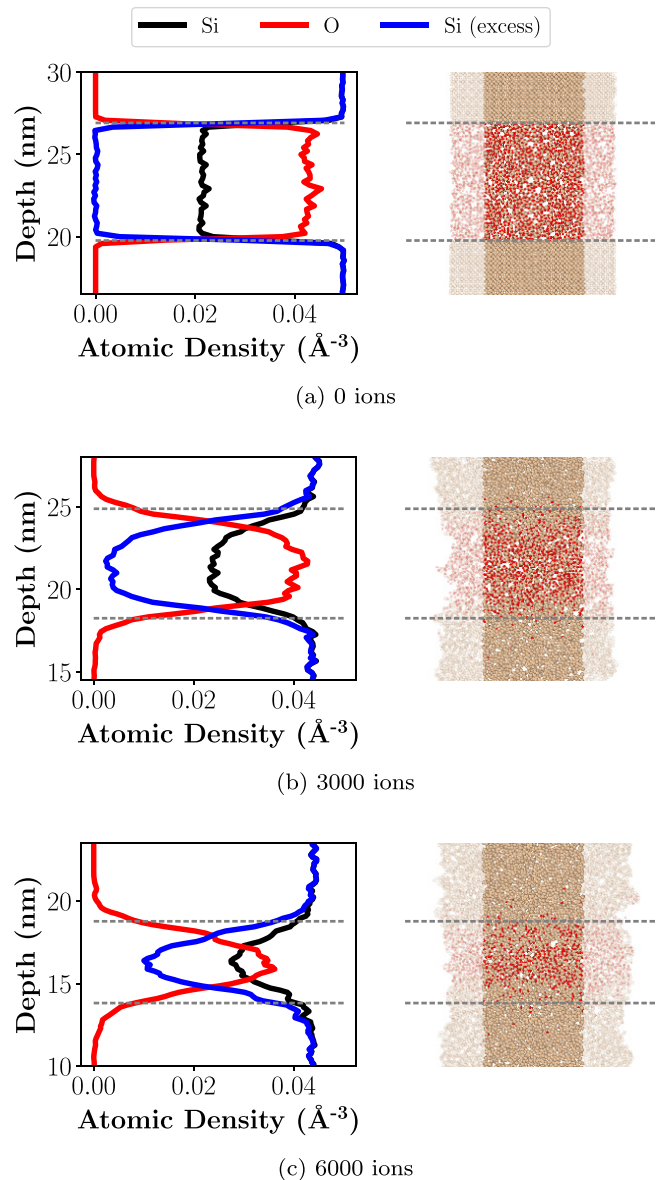


FIG. 2. The density profiles of the SiO<sub>x</sub> region at (a)  $0 \text{ cm}^{-2}$ , (b)  $3.8 \times 10^{15} \text{ cm}^{-2}$ , and (c)  $7.6 \times 10^{15} \text{ cm}^{-2}$ . On the left is the density profile and on the right a 1-nm-thick slice of the pillar. The horizontal gray dashed lines are showing the limits where SiO<sub>x</sub> drops below 10% of pure SiO<sub>2</sub>. “Excess Si” is a quantitative measure of the Si not bonded to two O atoms in the SiO<sub>2</sub> matrix. The analysis was done within the cylinder with  $r = 3$  nm (the areas excluded from the analysis are shown in transparent colors).

### B. Modification of atomic densities

We follow the formation of SiO<sub>x</sub> (where  $0 < x \leq 2$ ) by separately plotting the atomic densities of O and Si, and Si atoms not bonded to exactly two O atoms (hereafter called “excess Si”). Surface atoms are by nature more loosely bound than bulk atoms, which might lead to density artifacts at the surface caused by the irradiation. To exclude this uncertainty we only compared the atomic densities of the inner cylinder with  $r = 3$  nm as shown in Fig. 2 during the analysis.

The visible crystalline-to-amorphous phase transition in Figs. 2(a) to 2(c) explains the reduction in the atomic

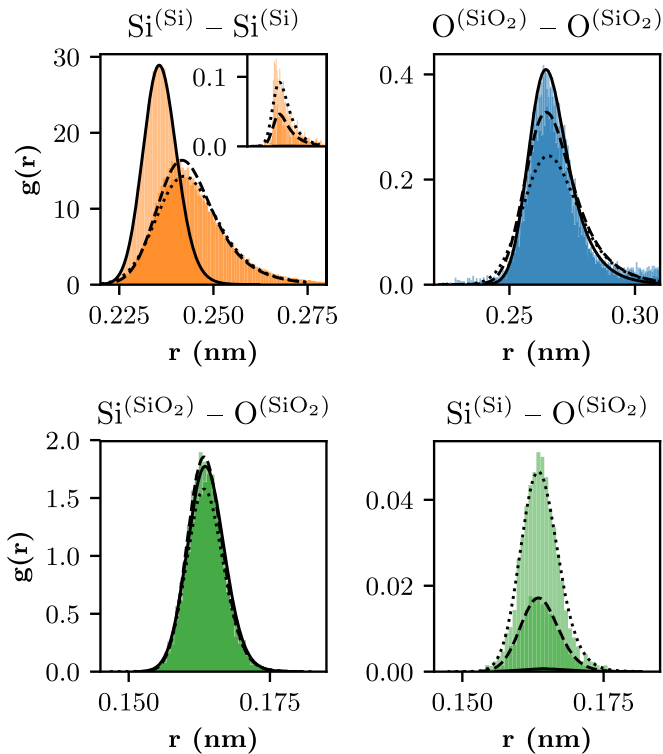


FIG. 3. PRDFs constructed pairwise for all atomic species in the nanopillar. The superscripts indicate the origin of the atoms: (Si) refers to the atoms of the original *c*-Si layers and (SiO<sub>2</sub>) refers to the species originating from the SiO<sub>2</sub> slab. Exponentially modified Gaussian fits outline the changes in the PRDFs with fluence: 0 cm<sup>-2</sup> is shown with the solid lines,  $3.8 \times 10^{15} \text{ cm}^{-2}$  with the dashed lines and  $7.6 \times 10^{15} \text{ cm}^{-2}$  with the dotted lines. The inset in the figure of Si<sup>(SiO<sub>2</sub>)</sup>-Si<sup>(SiO<sub>2</sub>)</sup> show the interactions of Si<sup>(SiO<sub>2</sub>)</sup>-Si<sup>(SiO<sub>2</sub>)</sup>. The interactions of Si<sup>(Si)</sup>-Si<sup>(SiO<sub>2</sub>)</sup> are omitted as they are very few compared to the other pairs and extremely similar in shape with the inset.

densities of the Si layers already after 3000 ions ( $0.047 \text{ \AA}^{-3}$  to  $0.042 \text{ \AA}^{-3}$ ).

We observed intensive atomic mixing with increasing fluence. The atomic density of the excess Si atoms grows rapidly even at the center of the SiO<sub>x</sub> layer. According to the authors of Ref. [14], the phase separation in SiO<sub>x</sub> at  $x \approx 1.0$  will lead to formation of a Si nanowire network within the SiO<sub>2</sub> matrix. While at  $x \approx 1.5$ , a QD of the right size can grow at the center of a 7-nm thick SiO<sub>2</sub> slice [16,35]. Hence we ran our high-fluence irradiation simulations until the  $x$  parameter in the middle of the SiO<sub>x</sub> layer was in the range between 1.0 and 1.5 (at the final ion fluence,  $x \approx 1.2$ ).

Figure 2 follows the overall atomic-mixing process in the nanopillar, but the details on the actual bonds forming during this period are not accessible in this particular data. To analyze the dynamics of Si-Si bonds growing within the SiO<sub>x</sub> layer during the irradiation, we plot the partial radial-pair-distribution functions (PRDFs)—with  $r_{\text{cutoff}} = 3.0 \text{ \AA}$ —for all atom-type pairs separately. The PRDF histograms corresponding to the three fluences shown in Fig. 3 were fitted with exponentially modified Gaussian distributions for analytical comparison of the dynamic changes with increasing fluence.

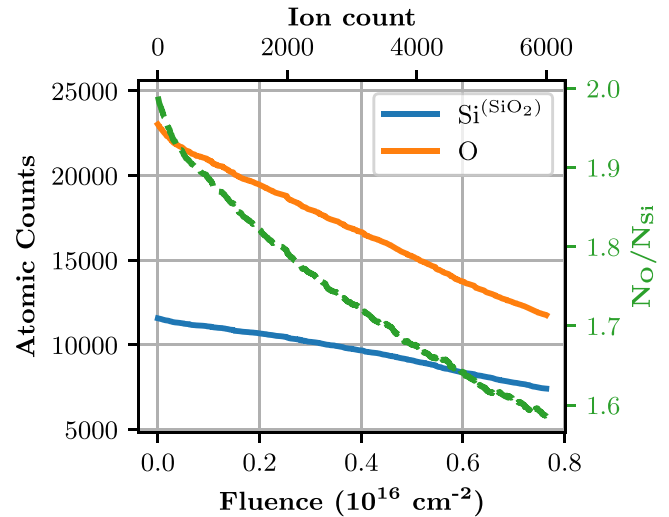


FIG. 4. Gradual decrease in absolute numbers of the Si<sup>(SiO<sub>2</sub>)</sup> and O<sup>(SiO<sub>2</sub>)</sup> atoms found within the pillar as a function of ion fluence. The dashed line shows the evolution of the relative content of the O atoms with respect to the Si atoms from the original SiO<sub>2</sub> slab:  $N_{\text{O}}/N_{\text{Si}}$ . Note the dramatic decrease of this ratio with increasing fluence, indicating preferential loss of O atoms from the system.

Hereafter, we use the superscripts to indicate the layer of the atoms' origin (initially, either Si or SiO<sub>2</sub>).

The shortening and broadening of the Si<sup>(Si)</sup>-Si<sup>(Si)</sup> peak indicates the crystalline-to-amorphous phase transition in the Si layers. We also observed a decrease in the PRDF showing the O<sup>(SiO<sub>2</sub>)</sup>-O<sup>(SiO<sub>2</sub>)</sup> bonds, which indicates an overall decrease of O atoms in the structure as well as their extensive spreading into the Si layers. A clear increase in the PRDFs of the Si<sup>(Si)</sup>-O<sup>(SiO<sub>2</sub>)</sup> bonds and a decrease in the PRDFs of Si<sup>(SiO<sub>2</sub>)</sup>-O<sup>(SiO<sub>2</sub>)</sup> bonds indicated successful atomic mixing, since more Si atoms from the Si layers were bonded with O atoms. The inset in the graph showing the Si<sup>(Si)</sup>-Si<sup>(Si)</sup> bonds shows the same PRDF for the Si<sup>(SiO<sub>2</sub>)</sup>-Si<sup>(SiO<sub>2</sub>)</sup>. These peaks appeared already at 3000 ions and continued to grow stronger throughout the simulation, indicating the inclusion of *a*-Si in the *a*-SiO<sub>x</sub> layer.

The significant decrease in the O-O and Si<sup>(SiO<sub>2</sub>)</sup>-O<sup>(SiO<sub>2</sub>)</sup> peaks over the fluence strongly show the general reduction of atoms in the nanopillar. To analyze whether this decrease is stoichiometric with respect to the number of Si atoms originally bonded with O atoms in the SiO<sub>2</sub> layer, we plot the fluence-dependent evolution of the absolute numbers of these atoms in Fig. 4. The comparison of the two curves shows a much faster decrease of O atoms compared to Si atoms originating from the same SiO<sub>2</sub> layer. The dashed green line shows  $N_{\text{O}}/N_{\text{Si}}$ , which is expected to fluctuate around 2.0 if both components are sputtered away with the same rate. However, we see that this value is rapidly decreasing, eventually reaching below 1.6. This analysis points to the preferential sputtering of O atoms compared to the Si atoms. This draws attention to the reduction of the relative number of O atoms, which will result in shrinkage of the SiO<sub>2</sub> slab during the postimplantation annealing. This unavoidable shrinkage must be taken into account when designing the embedded QD to maintain acceptable tunnel-junction distances [25].

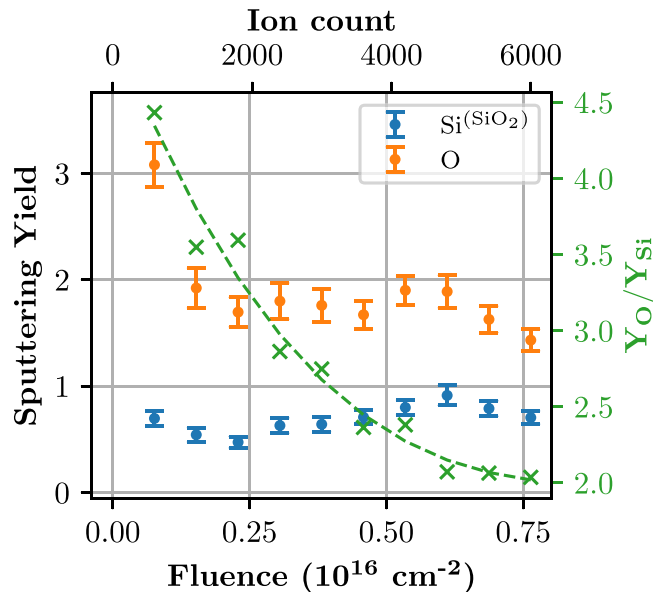


FIG. 5. The absolute sputtering yields of  $O^{(SiO_2)}$  and  $Si^{(SiO_2)}$  (left y-axis) and relative sputtering yield of  $O^{(SiO_2)}$  with respect to  $Si^{(SiO_2)}$ ,  $Y_O/Y_{Si}$  (right y-axis) as a function of fluence. At the beginning of the simulation the  $Y_O/Y_{Si} > 2$ , despite the molecular ratio of 2. The displayed values are averages from 600 consecutive ion events.

### C. Sputtering of the nanopillar

Irradiation of nanopillars by energetic ions will naturally lead to erosion of the structures by intensive sputtering. Hence, we estimate the sputtering contribution to the shortening of the nanopillar.

The high-energy cascades can intersect the extensive surface of a nanopillar in multiple locations. For instance, experimentally a threefold increase in sputtering yield has been observed for Si nanopillars when irradiated with  $Ne^+$  ions [35] and more than a 10-fold increase for  $Xe^+$  irradiation of Au nanorods [36]. The total sputtering yield on average during the entire irradiation simulation was  $12.74 \pm 10.87$ , where the standard deviation shows the major variation of all individual events. The sputtering yield is consistent with the value obtained in the TRY3DYN simulations reported in Ref. [35]. This high sputtering yield may indeed be the cause of the intensive material loss, however, more insights are needed to understand and confirm if the shape modifications are explained solely by the sputtering phenomenon. Moreover, the visual comparison of the three snapshots in Fig. 1 shows not only a shrinkage of the pillar but also a displacement of the  $SiO_x$  layer toward the base of pillar.

In Fig. 5 we show the evolution of the sputtering yields  $Y_{Si}$  and  $Y_O$  in absolute values (left y-axis) and as a relative value  $Y_O/Y_{Si}$  (right y-axis) with increasing fluence. We limited the analysis to the  $SiO_2$  slab to analyze the preferential sputtering of O atoms. Each data point is averaged over 600 consecutive ion events with the error bars indicating the standard error of the mean.

Figure 5 clearly shows the preferential sputtering of O atoms through the dramatic decrease in the  $Y_O/Y_{Si}$  ratio from more than 4 to almost exactly 2. The preferential sputtering of O atoms from  $\alpha$ - $SiO_2$  was also observed experimentally,

e.g., by Mizutani [37]. The high sputtering yield of the O atoms is explained by the lower cohesive energy in the  $SiO_2$  matrix (in the Watanabe-Samela potential, this is roughly half of the cohesive energy of Si, see, e.g., Ref. [38]). The  $Y_O/Y_{Si}$  ratio reduces with increasing fluence and eventually converges at  $\sim 2$ . The slowdown of the O sputtering rate may also be enhanced by the atom mixing during irradiation and intensive spread of O atoms outside of the  $SiO_x$  slab.

Although the preferential sputtering may indicate a more intensive loss of O atoms, for the purpose of the current study it is more important to know what is the O-to-Si ratio of the  $SiO_x$  matrix, including all Si atoms independently of their origin. In Fig. 6 we show the distribution of  $x$  in the  $SiO_x$  along the major axis of the pillar. We see that the maximum value of  $x$  is still close to 2 at  $3.8 \times 10^{15} \text{ cm}^{-2}$  fluence. However, at the final fluence of about  $7.6 \times 10^{15} \text{ cm}^{-2}$  the maximum  $x$  is close to 1 ( $\approx 1.22$ ). In the same graph we plot the distribution of the  $N_O/N_{Si}$  ratio, where both O and Si atoms originate from the  $SiO_2$  layer. In this plot we see that, while the  $x$  value decreases significantly in the middle of the  $SiO_2$  slab, the decrease of  $N_O/N_{Si} \approx 1.4$  is less dramatic at the final fluence. It is larger than  $x$  since it does not account for the mixed-in Si atoms from the surrounding  $c$ -Si layers. This suggests that the sputtering led to less dramatic change in the relative quantity of  $Si^{(SiO_2)}$  atoms than that of  $O^{(SiO_2)}$ . The numbers  $N_O/N_{Si} = 1.22$  and  $N_O/N_{Si^{(SiO_2)}} = 1.40$  demonstrate that only 13% of Si atoms do not originate from  $SiO_2$ . The reduction of the relative quantity of O atoms amounts to 39%, which is three times as high as the loss of Si atoms. This conclusion is also supported by the dynamic change in the sputtering yields of Si and O atoms (see Fig. 5). In this graph  $Y_{Si}$  does not change with the fluence after the initial drop, while the O atoms are sputtered less and less efficiently with increasing fluence.

### D. Ion hammering in Si/SiO<sub>2</sub>/Si nanopillars

In the following we address possible contribution to the nanopillar shape modification by the phenomenon, which is known as “ion hammering”—shrinkage of the irradiated material in the direction of the ion beam and subsequent broadening of it in the lateral directions. This phenomenon has been experimentally observed on the microscale in amorphous silica and silicon under high-fluence ion irradiation and explained by analytical means [39–42]. However, it has not been examined in detail with MD in a nanoscale system before.

If the shape change would depend entirely on intensive sputtering, there would be no lateral swelling as the large fraction of sputtering from the sides would cause a lateral thinning of the pillar along with the shortening from the top. However, Figs. 1(a) to 1(c) show a clear side-wise swelling when the pillar shrinks. To clarify the mechanisms leading to the observed shape modification of the nanopillar, we further analyze the atomic displacements of  $Si^{(SiO_2)}$  and  $O^{(SiO_2)}$ .

#### 1. Mean square displacement analysis

First of all, we analyze the spread of the atoms during the high fluence irradiation by plotting the mean square displacements (MSD) for all atoms of the nanopillar as a function of fluence in Fig. 7. We observed that the  $MSD^{(3)}$  of both  $Si^{(SiO_2)}$  and  $O^{(SiO_2)}$  grew dramatically with increasing fluence,

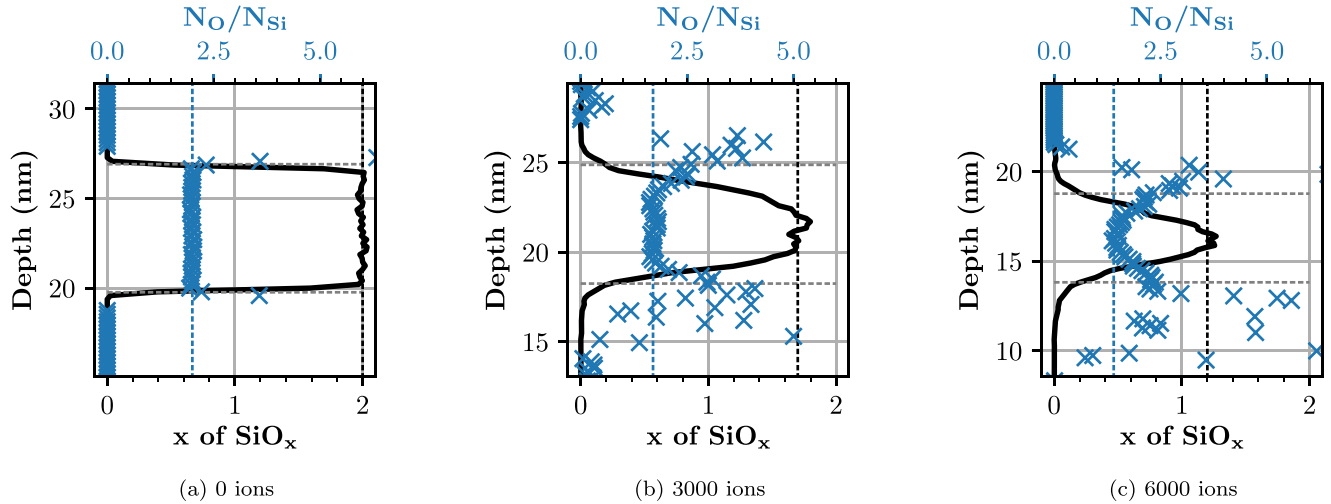


FIG. 6. Depth profiles of the relative content of the O atoms with respect to all Si atoms ( $x$  parameter of the  $\text{SiO}_x$  composition, bottom  $x$ -axis) as well as the relative content of the O atoms with respect to  $\text{Si}^{(\text{SiO}_2)}$  atoms only ( $N_{\text{O}}/N_{\text{Si}}$ , top  $x$ -axis) along the height of the pillar at three fluences: (a)  $0 \text{ cm}^{-2}$ ; (b)  $3.8 \times 10^{15} \text{ cm}^{-2}$ ; and (c)  $7.6 \times 10^{15} \text{ cm}^{-2}$ . The pure Si areas above and below the  $\text{SiO}_2$  slab are excluded in the figure. Note that  $N_{\text{O}}/N_{\text{Si}}$  increases at the interfaces, where the number of  $\text{Si}^{(\text{SiO}_2)}$  is very low.

however, their relative relationship over all fluences remained almost unchanged. The MSD was calculated as

$$\text{MSD}^{(m)} = \frac{1}{N} \sum_{i=1}^N |\vec{x}^{(i)}(f) - \vec{x}^{(i)}(0)|^2, \quad \vec{x} \in \mathbb{R}^{(m)}, \quad (1)$$

where  $N$  is the total number of the analyzed atoms, “0” and “ $f$ ” refer to the positions in the initial and the final frames at a given fluence, respectively; ( $m$ ) is the evaluated dimensionality.

The atomic mixing caused by the ballistic collisions in cascades can be interpreted as a random walk [27,43] with the coefficient similar to the diffusion coefficient in a thermally activated process. Associating the fluence of the constant flux

with time, and remembering that according to the Einstein relation for any random walk  $D = \text{MSD}/6t$  [44] one expects that the  $\text{MSD}^{(3)}$  must increase linearly with time, or with fluence under constant flux irradiation. However, the shape of the graphs in Fig. 7(a) describes a parabolic growth, which can be explained by a directional bias in the random walk.

Furthermore, by comparing the images in Figs. 1(a) and 1(c) we notice that the entire  $\text{SiO}_x$  slab is dramatically shifted downward, i.e., in the direction of the ion beam. It is obvious that this shift causes the expected bias in a single direction, altering the behavior of the MSD for the atoms in the  $\text{SiO}_x$  slab. The closely following trends of the  $\text{MSD}^{(1)}$  and  $\text{MSD}^{(3)}$  along the  $z$ -axis in Figs. 7(a) and 7(b) for  $\text{Si}^{(\text{SiO}_2)}$  and  $\text{O}^{(\text{SiO}_2)}$  atoms separately confirms this dependence. The maximum MSD in

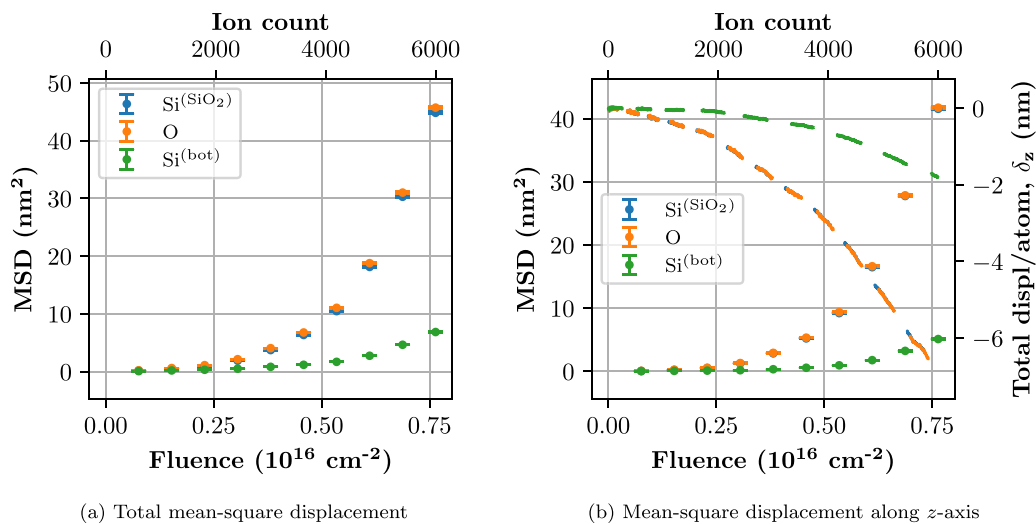


FIG. 7. Mean-square displacements (MSD,  $\text{nm}^2$ ) of  $\text{Si}^{(\text{SiO}_2)}$  and  $\text{O}^{(\text{SiO}_2)}$  calculated according to Eq. (1) for different dimensions: (a) compares  $\text{MSD}^{(3)}$  for both species in the 3D geometry; (b) show separately out-of-plane  $\text{MSD}^{(1)}$  and in-plane  $\text{MSD}^{(2)}$  with respect to the slab geometry, respectively, for both species. The dashed lines show the total displacement (the right y-axis). The  $\text{MSD}^{(1,3)}$  include the downwards shift of the  $\text{SiO}_x$  slab as a whole. In both graphs we plot separately the Si atoms, which originated from the bottom layer ( $\text{Si}_{\text{bot}}$ ). The data points are calculated averages from 600 consecutive ion events.

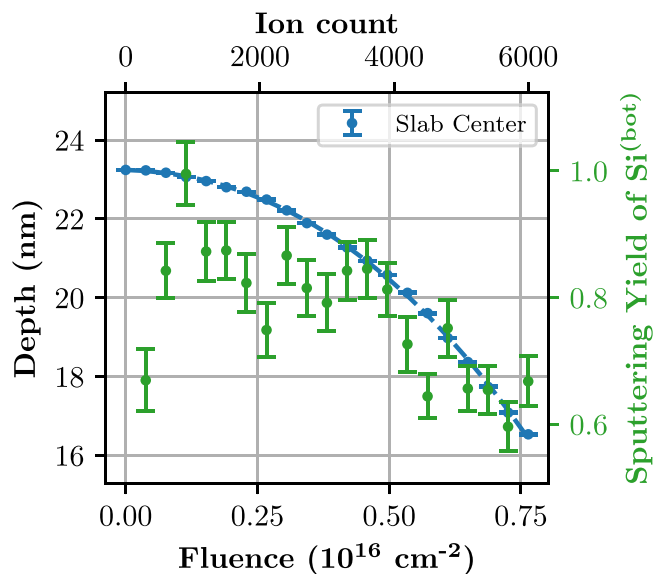


FIG. 8. The change of the  $\text{SiO}_2$  slab thickness over time. The upper and lower limits of the  $\text{SiO}_x$  region are located where the concentration of  $\text{SiO}_2$  drops below 10%. The data points are averages from 300 consecutive ion events.

these graphs is about  $40 \text{ nm}^2$ . By taking the square root of this value we obtain a rough estimate of the directional bias, which amounts to  $\sqrt{\text{MSD}} \approx 6.3 \text{ nm}$ . Comparing the midpoints of the  $\text{SiO}_x$  layers in the images of Figs. 1(a) and 1(c), we will arrive at approximately the same value of about 7 nm. This result clearly indicates that the ion hammering effect took place in our high-fluence ion-irradiation simulations. The parabolic behavior of  $\text{MSD}^{(1)}$  can be explained by the linear growth of the  $z$ -component of the total displacement of the atoms in the system. We calculate this value for all  $\text{Si}^{(\text{SiO}_2)}$  and  $\text{O}^{(\text{SiO}_2)}$  atoms as a function of fluence as

$$\delta_z = \frac{1}{N_{\text{displaced}}} \sum_i^{N_{\text{displaced}}} [z^i(f) - z^i(0)], \quad (2)$$

where  $i$  is the current atom [45]. We plot this value in Fig. 7(b) with the reference to the right  $y$ -axis.

Since the  $z$ -axis is directed upward along the major axis of the pillar, the growth of this component is towards negative values. It is rather natural to expect that the significant shift of the  $\text{SiO}_x$  layer as a whole in the direction of the ion beam will result in a linear growth of  $\delta_z$ , nonetheless, we observe that this growth is rather superlinear. In the following, we address the effects that may explain this superlinearity.

One of the possible reasons for the dramatic shift of the  $\text{SiO}_x$  slab as a whole may be the sputtering of Si atoms from the bottom layer of the pillar. Hence, we plot the sputtering yield of these atoms and the absolute position of the middle of the  $\text{SiO}_x$  slab in the same graph as functions of ion fluence (see Fig. 8). The sputtering yield  $Y_{\text{Si}}^{\text{bot}}$  is calculated similarly to  $Y_{\text{Si}}$  and  $Y_{\text{O}}$  (see Sec. III C), but by averaging over 300 consecutive ion events. The total displacement of the slab amounts to 7 nm, which is consistent with the estimate of  $\sqrt{\text{MSD}^{(3)}}$  from Fig. 7(a).

It is worth noting that the 25 keV  $\text{Si}^+$  ions generate most efficiently recoils in pure Si at depths of 20 nm to 30 nm from the surface according to SRIM2013 estimates [31]. At the beginning of the simulation, the combined height of the upper  $c$ -Si layer and the  $a$ - $\text{SiO}_2$  slab is 32 nm, which coincides well with the ion range. The shorter the nanopillar becomes, the deeper the atomic cascades penetrate. This leads to stronger involvement in the cascades and, subsequently, higher sputtering yields of the atoms from the bottom layer at higher fluences. The sputtering yield saturates at about  $Y_{\text{Si}}^{\text{bot}} \approx 8.5$  atoms/ion when the cascades fully reach the bottom  $c$ -Si layer and the atoms begin to sputter from the entire surface area around this layer.

The subsequent shrinkage of the pillar reduces the surface area of the bottom layer as well [cf. the size of the bottom layer at the beginning of the simulations, 19 nm in Fig. 1(a) and  $\sim 13$  nm in Fig. 1(c)], reducing the surface area available for sputtering and, hence, reducing  $Y_{\text{Si}}^{\text{bot}}$ .

If the downshift of the  $\text{SiO}_x$  slab was only due to the sputtering of  $\text{Si}^{\text{bot}}$  atoms, it should have slowed down following the slowdown of  $Y_{\text{Si}}^{\text{bot}}$ . However, Fig. 8 reveals the opposite trend: the slab shifts down even faster at this stage of the irradiation. This means that the shift of the slab is not only due to removing the atoms from the bottom layer, but due to the pressure (ion hammering) exerted on the pillar by the ion irradiation. This explains the superlinear behavior of the  $z$ -component of the total displacement  $\delta_z$ , which results from the superposition of the sputtering of the  $\text{Si}^{\text{bot}}$  atoms and the ion-hammering phenomenon.

We also plotted the  $\text{MSD}^{(3)}$  and  $\text{MSD}^{(1)}$  for the  $\text{Si}^{\text{bot}}$  in Figs. 7(a) and 7(b), respectively. Although the increase of these values is much slower than for  $\text{Si}^{(\text{SiO}_2)}$  and  $\text{O}^{(\text{SiO}_2)}$ , it is clear that  $\text{Si}^{\text{bot}}$  also experiences an overall downward movement because of the ion hammering since  $\text{MSD}^{(1)}$  is only slightly smaller than  $\text{MSD}^{(3)}$ , but much smaller than  $\text{MSD}^{(1)}$  for the atoms of the slab.

## 2. Lateral displacements of the $\text{SiO}_x$ atoms

A significantly faster growth of  $\text{MSD}^{(2)}$  for O atoms compared to the Si atoms [see Fig. 9(a)] indicates that the O atoms move further than the Si ones during cascades. We do not notice this tendency in the  $z$ -direction since the displacement in this direction is driven by the shift of the entire slab.

Unlike the  $\text{MSD}^{(3)}$ , the fluence dependence of  $\text{MSD}^{(2)}$  is very close to linear. The  $\text{MSD}^{(2)}$  values for both O and Si atoms grow rapidly up to relatively high fluence. At  $\sim 6 \times 10^{15} \text{ cm}^{-2}$  fluence the slope changes and the  $\text{MSD}^{(2)}$  for both atom species grow even faster. The change of the slope [seen as a somewhat superlinear behavior of the  $\text{MSD}^{(2)}$  in Fig. 9(a)] is explained by a gradual decrease of the nanopillar height with the fluence. Eventually the cascades begin to overlap stronger with the  $\text{SiO}_2$  slab, increasing the energy transfer in this region and, hence, affecting the linear growth of  $\text{MSD}^{(2)}$  of  $\text{Si}^{(\text{SiO}_2)}$  and  $\text{O}^{(\text{SiO}_2)}$  with the fluence. This trend is even more strongly pronounced for the  $\text{Si}^{\text{bot}}$  atoms, where the effect of the cascade overlap with this region is slightly slower.

The previous conclusion agrees well with the results shown in Fig. 5. A small increase in the sputtering yield for both  $\text{Si}^{(\text{SiO}_2)}$  and  $\text{O}^{(\text{SiO}_2)}$  is also observed at  $\sim 6 \times 10^{15} \text{ cm}^{-2}$ . The

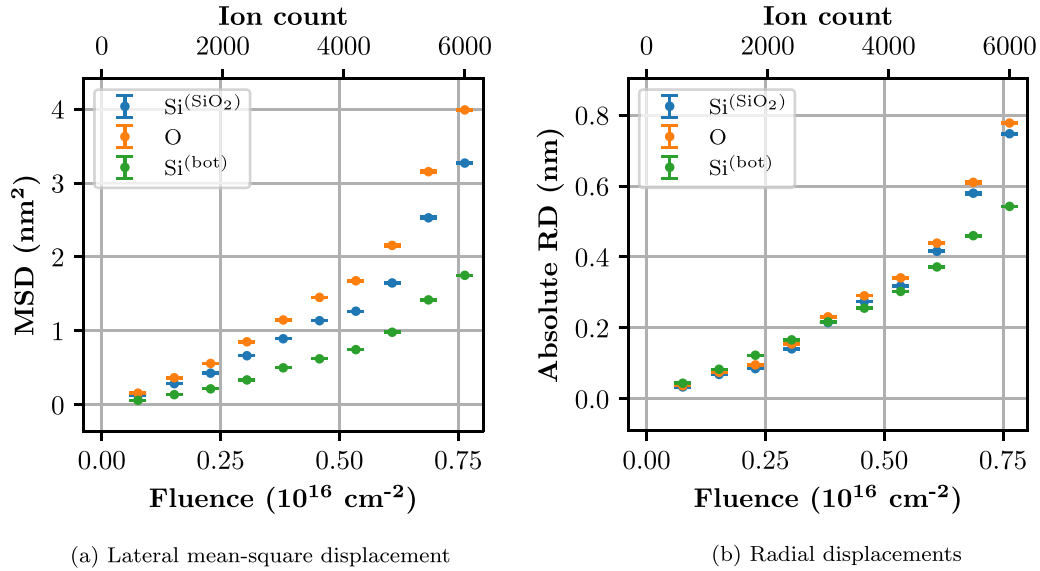


FIG. 9. Displacements of  $\text{Si}^{(\text{SiO}_2)}$  and  $\text{O}^{(\text{SiO}_2)}$  atoms in lateral directions. Panel (a) shows the  $\text{MSD}^{(2)}$  and panel (b) the absolute values of atom displacements calculated according to Eq. (3) separately for  $\text{Si}^{(\text{SiO}_2)}$  and  $\text{O}^{(\text{SiO}_2)}$  atoms. The positive values of radial displacements indicate the tendency towards the outer rim of the pillar. The  $\text{O}^{(\text{SiO}_2)}$  atoms are displaced slightly further than  $\text{Si}^{(\text{SiO}_2)}$  atoms [see (a)]. The data points are calculated as averages of 600 consecutive ion events.

rapid increase of the  $\text{MSD}^{(2)}$  does not yet reveal directional preference of atomic displacements in the cascades. This is why we also plot the absolute radial displacement, RD, of the  $\text{Si}^{(\text{SiO}_2)}$  and  $\text{O}^{(\text{SiO}_2)}$  atoms in Fig. 9(b), which was calculated as

$$\text{RD} = \frac{1}{N} \sum_{i=1}^N (|\vec{x}^{(i)}(f)| - |\vec{x}^{(i)}(0)|), \quad \vec{x} \in \mathbb{R}^2, \quad (3)$$

[see Eq. (1) for descriptions of the variables].

The positive values of RD [see Fig. 9(b)] indicate that both Si and O atoms on average are always displaced outwards from the major axis of the pillar. Note that O atoms are displaced only slightly stronger than Si atoms. In these graphs, we also note the same tendency for superlinearity of the atom displacements when the cascades overlap more with the  $\text{SiO}_x$  slab as seen in Fig. 9(a).

### 3. Bell-like shape of irradiated nanopillar

The combination of strong displacement along the main axis of the pillar and the positive radial displacements of atoms in the nanopillar already manifest the presence of the ion-hammering effect. However, in the recent experiments by Xu *et al.* [35], the shape of the nanopillars became bell-like after prolonged irradiation at room temperature as seen in Fig. 10.

The snapshots shown in Fig. 1 do not exhibit a similar tendency toward forming the bell-like shape around the nanopillar base as seen in the experiments. The relatively small pedestal (limited substrate area) and the invariable irradiation spot used for efficiency reasons in the simulations of the tall nanopillar might have introduced artifacts confounding the natural geometry development caused by the irradiation. For example, redeposition of sputtered atoms may play a substantial role in shape modification on nanoscale

[46], however, due to the small pedestal, we were not able to follow the trajectories of the sputtered atoms reaching the substrate.

In the following, we will look in detail at the possible effects of the redeposition as well as the plastic flow as response to a single atomic cascade triggered by an incoming ion, excluding possible diffusional displacements, which may enter the analysis performed in Sec. III D 2.

### 4. Redeposition of sputtered atoms

To estimate the effect of the redeposition of sputtered atoms, we analyzed the polar angle distributions and the distributions of the origin ( $z$ -coordinate) of the sputtered atoms. The polar angle  $\theta$  was measured from the  $z$ -axis aligned with the major axis of the pillar and directed upwards. By

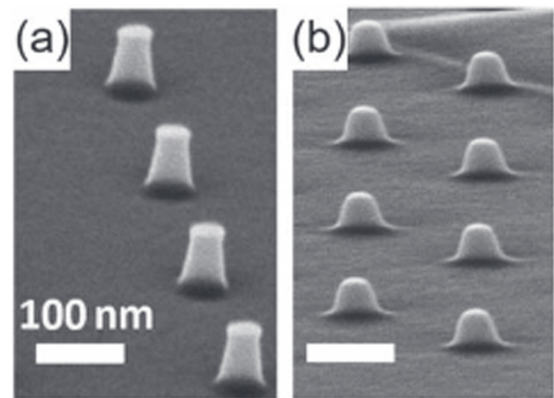


FIG. 10. Experimental images of a Si pillar irradiated by 25 keV  $\text{Ne}^+$ . The images are taken at  $85^\circ$  using  $\text{He}^+$  with a helium ion microscope. Panel (a) shows the unirradiated pillar and panel (b) the pillar after  $2 \times 10^{16} \text{ cm}^{-2}$  fluence at room temperature. The figure is from Ref. [35], reproduced under the CC-BY license.



averaging these quantities for the atoms sputtered within three subsequent groups of 2000 consecutive impacts, we were able to follow the dynamics of the changes in these distributions with fluence.

Moreover, we plotted these distributions distinguishing between the ballistically sputtered atoms ( $E_{\text{sput}} > 15 \text{ eV}$ ) shown in Fig. 11(a), and the low energetic sputtered atoms ( $E_{\text{sput}} \leq 15 \text{ eV}$ ) shown in Fig. 11(b). The last equation resulted from multibody collisions of the atoms in the surface layers or of the atoms loosely bound at the surface. Directions of the ballistically sputtered atoms are mainly determined by binary collisions, while we associate the low energetic sputtered atoms with thermal sputtering since the direction of their movements is random.

A comparison of Figs. 11(a) and 11(b) shows that the amount of ballistically sputtered atoms is significantly lower than of those that sputtered thermally. Although the ballistically sputtered atoms move preferentially downwards (towards redeposition) with the peak at  $\theta \approx 120^\circ$ , this trend is overtaken by the thermally sputtered atoms with nearly equal probability to fly upward (away from the nanopillar and the substrate) and downward (to the surface of the substrate). There is also no significant change in this trend with increasing fluence. The distributions centered at  $\theta = 90^\circ$  show that the thermal sputtering takes place mainly at the sides of the pillar. A slight skewness to the left ( $\theta < 90^\circ$ ) is explained by the contribution of the processes at the very top of the nanopillar.

The nearly symmetric shape of the polar angle distributions around  $90^\circ$  mean that at least half of the sputtered atoms will redeposit around the base of the pillar.

Figure 11(c) shows the evolution of the origins of the sputtered atoms. Again we see a strong contribution of side sputtering while the number of atoms sputtered from the top of the pillar is insignificant. The redeposition contribution to the total shape modification will increase with higher fluence as the origin of the sputtered atoms gets closer to the bottom of the pillar. The two distinct peaks of the first distribution are explained by ion channeling [47] through the top *c*-Si slab before it was rendered fully amorphous.

These results indicate that redeposition, contributing to the shape modification might have taken place. However, the total amount of sputtered atoms with significant probability for redeposition is insufficient to cause the significant shape modifications observed in the experiments (cf. Fig. 10).

### 5. Plastic flow in individual cascades

We further investigate the nanoscale ion hammering by studying the atom displacement field and the plastic flow caused by a single cascade event. Atom displacements below  $0.6 \text{ \AA}$  are related to thermal vibrations and can be omitted in the analysis, as they are too short to contribute meaningfully to the plastic flow. Atom displacements above  $1.5 \text{ \AA}$  can be ignored as they are longer than the bond length in the Si matrix, and as such they have already been knocked further than the relaxation can force them. Only the displacements within these margins will indicate whether there are small

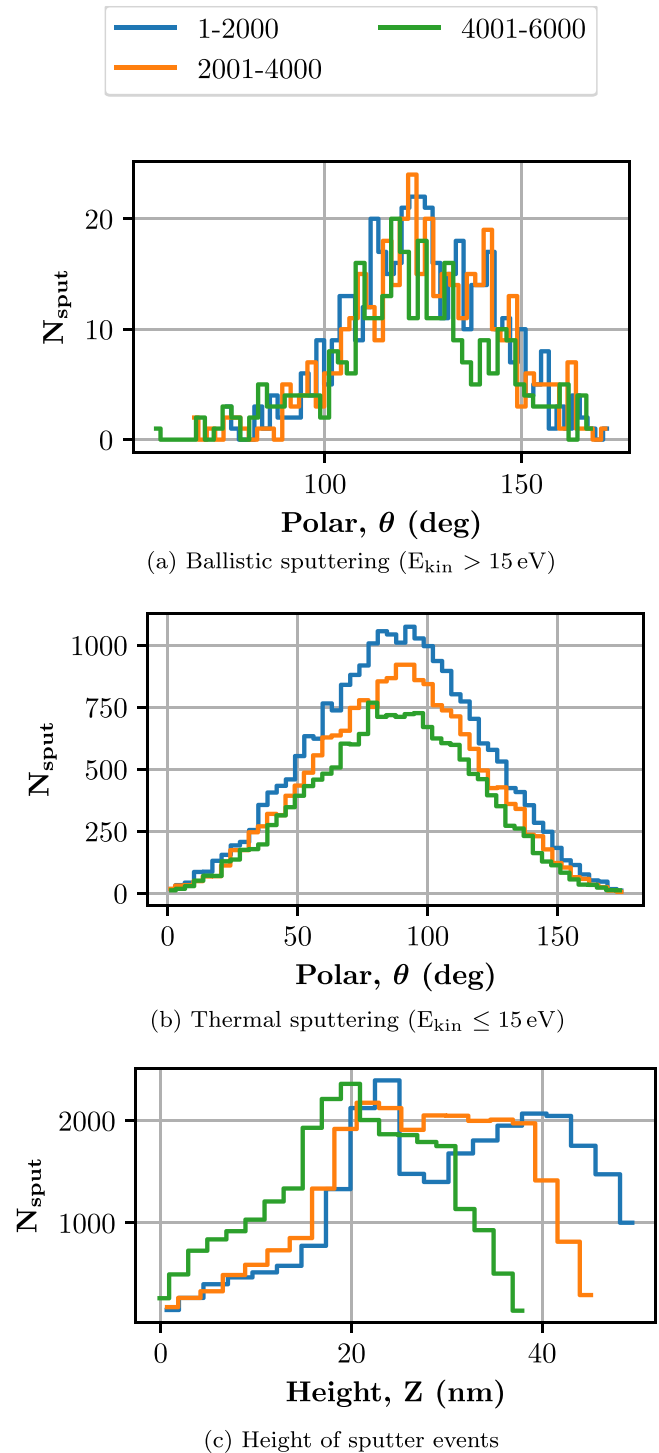


FIG. 11. Polar angular distribution of the sputtered atoms. Statistics are collected over all fluences for all sputtered atoms. The angle is counted from the  $z$ -axis, so that the angle of  $90^\circ$  shows the direction parallel to the surface of the pedestal. Panel (a) shows the distribution of ballistically sputtered atoms with the kinetic energy above 15 eV and panel (b) shows the thermally sputtered atoms with the kinetic energy below or equal to 15 eV. (c) shows the height of the sputtering events. As the pillar shrinks, the distribution of the atoms moves to the left. Each histogram includes the sputtered atoms in two thousand consecutive ion impacts.

displacements surviving the postcascade relaxation. Such displacements accumulated in many subsequent cascades (as we previously showed with a different geometry in Ref. [45]) can contribute to permanent shape modification causing the effect known as ion hammering.

Figure 12 shows the mean and standard deviation of ten individual cascade simulations, with randomly chosen entry points within one unit cell above the lateral center of the pillar. The displacements are compared to the initial positions of the atoms, i.e., before the ion cascade has started. We removed all sputtered atoms, using OVITO as mentioned in Sec. II B. Since all simulations in this work were performed at normal ion incidence, we analyzed the atomic displacements in the cascades directing the ions both at  $0^\circ$  and  $7^\circ$  to the main axis of the pillar. The later angle was added to assess the effect of ion channeling on the atomic displacements. The cascades were allowed to develop for 3 ps in the NVE ensemble before quenching the temperature towards the initial temperature for another 2 ps. The temperature control was applied as in the rest of the simulations.

To analyze the atomic displacements in both a crystalline and an amorphous system, we chose two snapshots of the tall nanopillar, the pristine and one after 3000 consecutive ion events. The second structure was selected for the amorphous case study since the Si layers in the nanopillar had already lost the crystallinity, but the overall shape had not yet been dramatically modified. We plot the total lateral displacements of the atoms in Fig. 12(a) and the sum of all displacements along the major axis of the nanopillar in Fig. 12(b) separately for all case studies. In both figures we see that the amorphous system is much more susceptible to atomic displacements than the crystalline one. Moreover, we see in Fig. 12 that the largest displacements appear within and beneath the  $\text{SiO}_2$  region, which is contrary to the displacements in the crystalline structure.

We simulated the cascades in crystalline and amorphous structures at the same incident angles,  $0^\circ$  and  $7^\circ$ , respectively. The later angle allowed avoiding channeling in the upper c-Si layer. Although some bias in the displacement distributions can be expected in amorphous structures under the  $7^\circ$  tilt of the ion beam, we have not seen any notable difference between the  $0^\circ$  and  $7^\circ$  irradiation scenarios. The  $7^\circ$  tilt in incidence during irradiation of the crystalline structure led to an increase of the total displacements in the upper Si layer due to stronger energy transfer in this layer. However, the trend disappeared completely at the depth of  $\alpha\text{-SiO}_2$  and below it, where the displacements of atoms compared closely to those obtained at normal incidence (compare the blue and orange curves in Fig. 12  $\lesssim 300$  Å). This observation makes it clear that amorphous structures are more prone to allow for atomic flow than crystalline structures, where the atoms are organized in periodic lattices. Moreover, there are practically no significant lateral displacements in crystalline structures, which possibly may lead to side-wise plastic flow, see Fig. 12(a).

We also note that the atomic displacements along the major axis of the pillar [Fig. 12(b)] are stronger than the lateral displacements [Fig. 12(a)] since the momentum transfer from the ions to the atoms of the pillar occurs mainly in the direction of the beam. Clearly both types of displacements are stronger in the upper Si layer in the crystalline nanopillar (see the case of

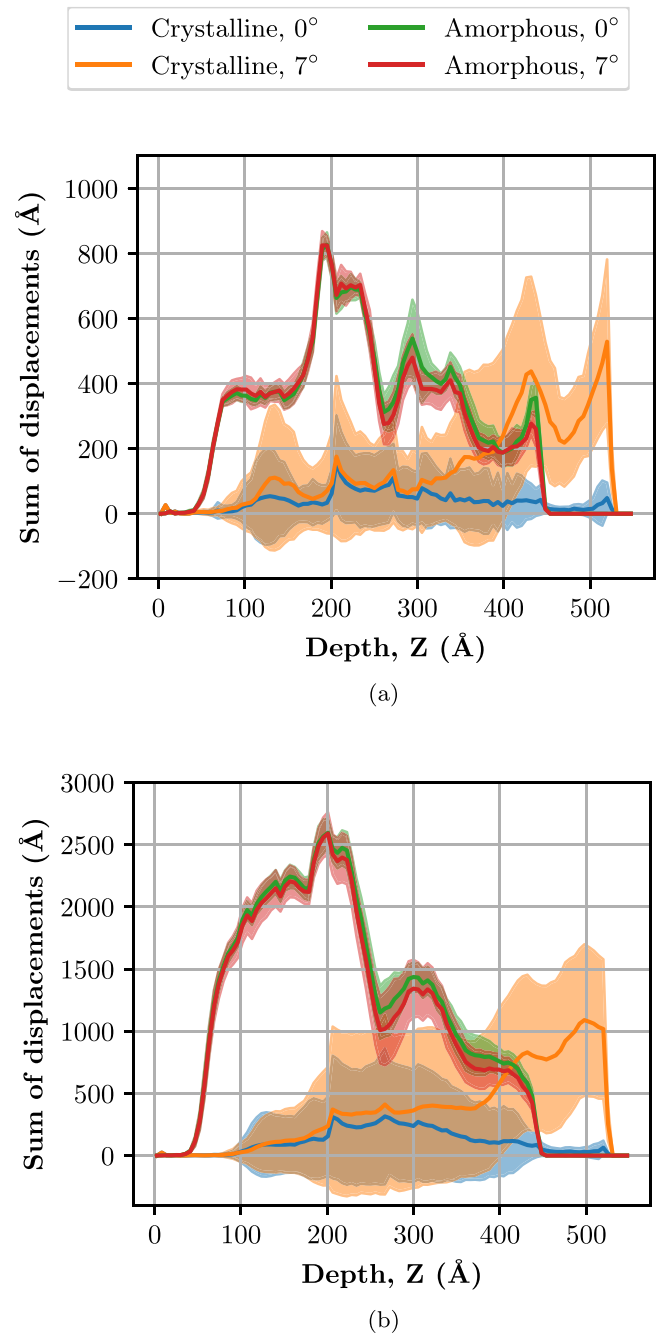


FIG. 12. Distribution of the total displacement of atoms along the major axis of the pillar averaged over ten independent single cascade simulations. The distributions show how the stress affects the relaxation of the lattice. The  $0 \text{ cm}^{-2}$  frame was used as reference for the crystalline structure and the  $3.8 \times 10^{15} \text{ cm}^{-2}$  was used as reference for the amorphous structure. Panel (a) shows the lateral distribution of the total displacement and panel (b) shows the distribution of the total displacement in the nanopillar along the major axis. The separate case with a slightly off-normal direction of incidence shows that the channeling effects do not affect the outcome of these simulations.

$7^\circ$  incidence in Fig. 12), while in the amorphized nanopillar the atoms are displaced much stronger, closer to the bottom of the pillar. This finding indicates a much stronger long-range flow as a response to the stress induced by a single cascade in the amorphous structure compared to the crystalline one.

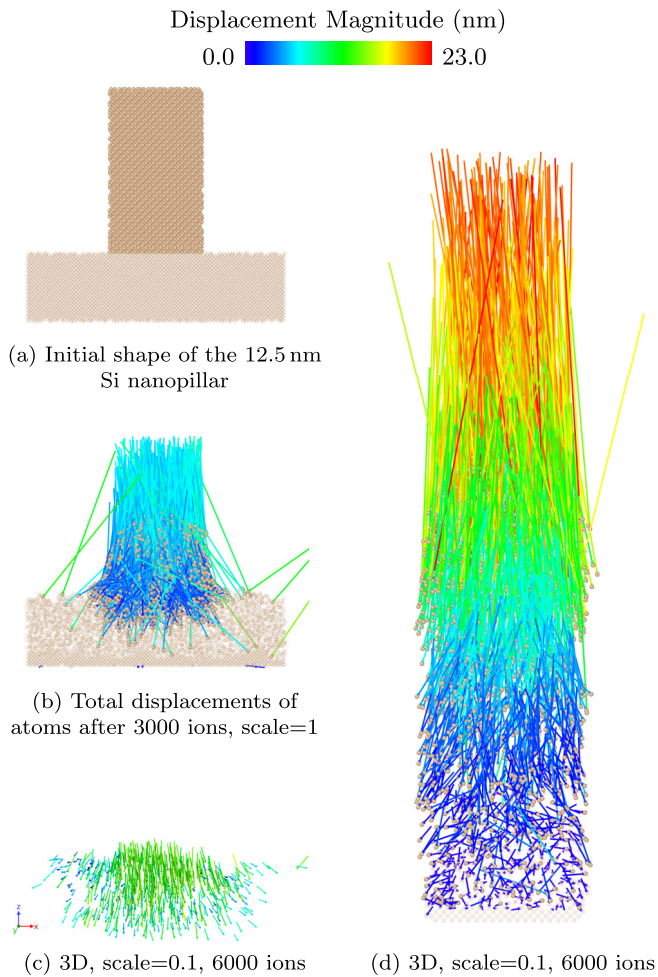


FIG. 13. Total displacements of atoms indicating the ion hammering effect. Figures (a) to (c) are from a  $5 \text{ \AA}$  thick slice at the center of the pillar with reduced size. Panel (a) shows the relaxed  $12.5 \text{ nm}$  Si pillar before any irradiation, panel (b) the total displacement vectors after 3000 ions, and panel (c) 6000 ions. The displacement vectors in (c) are scaled down and shown as 10% of the original size. The total displacements of the atoms in a  $1 \text{ \AA}$  slice after 6000 ions in the Si/SiO<sub>2</sub>/Si nanopillar is shown in (d). The displacements were computed with OVITO's displacement modifier.

### E. Deformation of the short nanopillar

To analyze the plastic flow further, we illustrate the dynamics of the process in three snapshots of the irradiation process of the short nanopillar in Figs. 13(a) to 13(c). We show only the central slices of the thickness of  $5 \text{ \AA}$ . The displacement vectors point from the initial position to the current position of the atoms. A video of the nanopillar shape evolution during the entire irradiation process is available in the Supplemental Material [48]. In this video we first observe the crystalline-to-amorphous phase transition, after that we see how the pillar gradually assumes a bell shape and later eventually flattens down completely. In this movie, it is also clearly visible that the bell shape does not develop until the atoms near the bottom of the pillar get involved in the cascades more strongly.

In Fig. 13(b) we see a strong downward displacement of the atoms in the upper part of the pillar. However, the atoms

located closer to the base of the pillar are displaced more randomly with a clear preference towards the cylindrical surface of the pillar, eventually contributing to the formation of the bell shape. We also notice that some of the displacement vectors connected atoms from the top of the pillar to the surface of the pedestal. These indicate redeposition cases of the sputtered atoms. Note that the figure only shows the redeposition events from a thin slice of the system.

Figure 13(c) shows the final stage after 6000 ions. The short nanopillar is flattened and the total displacements of the atoms remaining in the system show that the atoms are not just sputtered, but also forced deeper into the substrate. In Fig. 13(d) we present the atom displacements of the large nanopillar at 6000 ions [cf. Fig. 1(c)] compared to the unirradiated stage. In this figure we see the top atoms are again displaced downward much stronger and more or less straight with a slight tendency of side-wise broadening. However, the lower the atoms are located, the more random their displacements become.

During the ion impact the momentum is transferred to the atoms through high-kinetic collisions in the direction of the incoming ion. This explains the strong downward displacement of the atoms located in the upper part of the pillar. The atoms located closer to the bottom were mainly involved in the low-energy multibody interaction part of collision cascades, where the random walk component of atom movements becomes prominent. This behavior is more visible when plotting the atomic displacements between shorter intervals of consecutive ion impacts as in Fig. 14, where we show a sequence of images to demonstrate the correlation between the shape evolution of the pillar and the corresponding atomic displacements from the previous frame (the frames were recorded after every 500th impact). In these images (where the thickness of the slices plotted was reduced to  $2 \text{ \AA}$  for clarity) we see that the top atoms move dominantly downwards, while the lower atoms move more randomly, with somewhat preferred side-wise direction. This preferential direction may be explained by lower barriers for the atomic random walk in the direction of the open surface as well as relaxation of the built-up stresses from the cascades and the initial downward motion of the upper layers.

Recent work shows that the relaxation in amorphous material is continuous and proceeds through very small displacements ( $<1 \text{ \AA}$ ) [45]. These tiny displacements, however, can contribute strongly to the macroscopic shape modification of the amorphous material under prolonged ion irradiation. This is clearly visible at the last stage of the irradiated short nanopillar shown in Fig. 13(c). Here we see that the atoms that originally constituted the pillar, are pressed into the substrate, and that the strong displacement vectors are surrounded by smaller displacements caused by the relaxation and slightly biased diffusion-like atomic movements. Therefore, we conclude that the incoming ions induce a strong displacement of the top atoms downward and into the material, inducing stress, that tends to relax towards the open surface at the sides of the pillar. These small relaxation displacements superpose with the random walk displacements in the low-energy (peripheral) parts of the cascades, leading to the phenomenon known as the ion-hammering effect.

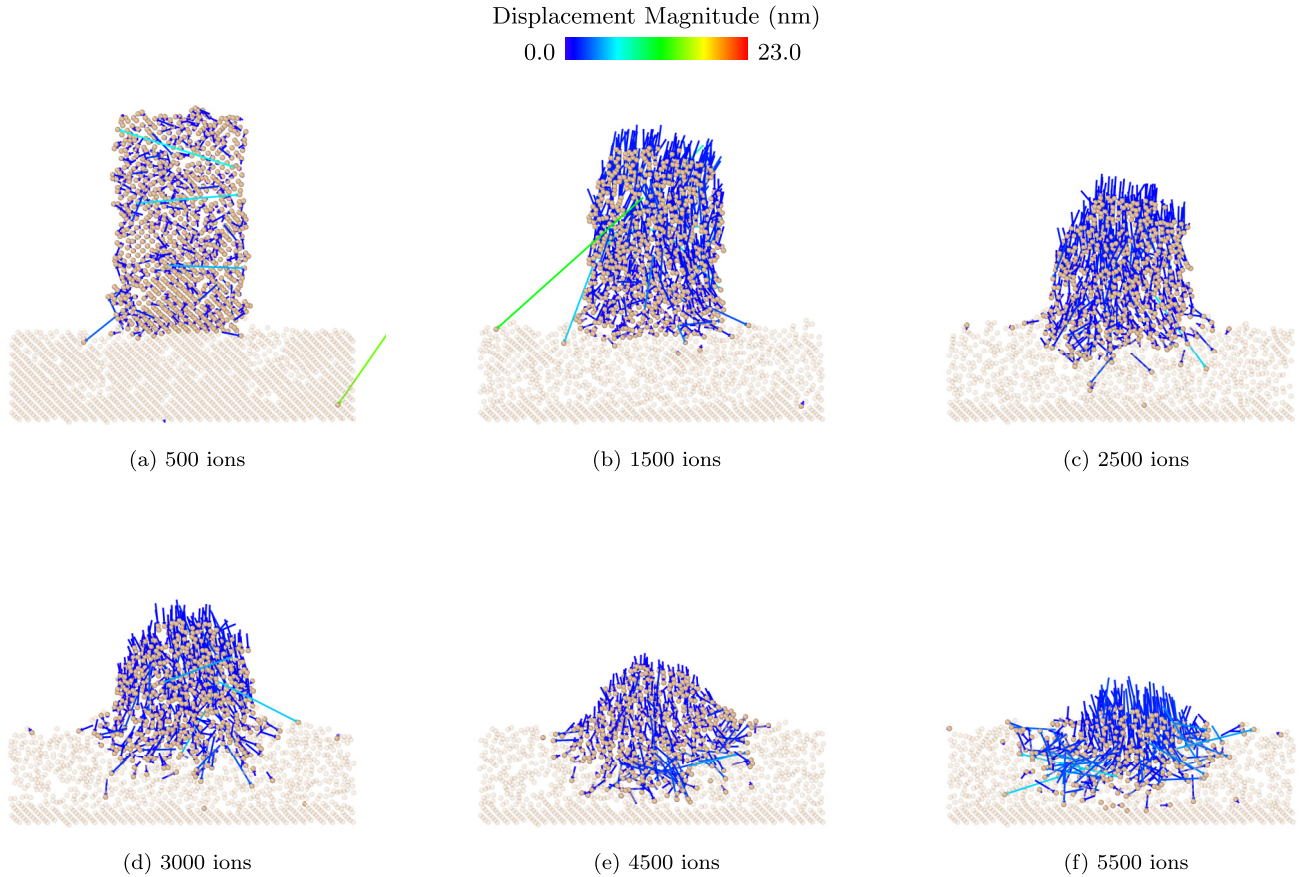


FIG. 14. Sequence of the shape modification of the 12.5-nm Si pillar. The displacement vectors connect the position of the atoms at intervals of 500 ions (some intermediate stages are not shown).

The same effect was observed in the tall nanopillar shown in Fig. 13(d). This observation explains why the tall nanopillar shown in Figs. 1(a) to 1(c) did not develop the bell-like shape. Since the cascades, even at the end of the simulations, barely reached the bottom region of the pillar, the displacements near the base of the pillar are still very small.

Since the processes of thermal diffusion are too slow for the MD timescale, the shape of the irradiated nanopillars may also be explained by enhanced surface diffusion under irradiation. To verify this hypothesis, we analyzed the displacements of the inner and outer atoms separately. Larger displacements of surface atoms may indicate the higher activity of these atoms, which at longer timescales may contribute to surface modification via enhanced surface diffusion.

In Fig. 15, we show separately the total (3D, solid lines) and lateral (2D, dashed lines) displacement distributions for the outer (orange color) and inner (blue color) atoms. Since the definition of atoms as inner and outer is somewhat arbitrary, we show the histograms of three different inner/outer radii pairs in Fig. 15. The inset at the top right corner of each subfigure shows the cross section of the nanopillar with the atoms colored according to the chosen radii-combo used in the corresponding histograms. Although the distributions for the outer atoms have longer tails toward larger displacements, the distributions appear to be rather similar. This result indicates that even though there is slightly stronger displacement

of the outer atoms compared to the inner ones, all the displacements are the results of a random walk of similar nature and only the atoms that could have been sputtered near the surface of the pedestal could contribute to the formation of a bell-shaped outskirts of the pillar. This is consistent with the experimental images, where the broadening appears only at the base of the pillar after the pillar became sufficiently short for the collision cascades to develop near the base.

#### F. Summary of shape modification analysis

By briefly going over all the results in this section, we find that broadening of the pillar appears only in the amorphous phase due to numerous small displacements surviving after the collision cascade has faded. The distribution of the total displacement along the nanopillar at the end of the relaxation phase shows the long-range plastic flow in amorphous material along the ion-beam direction, and laterally in response to the effect of the ion cascades. The flow is stronger near the substrate, causing thickening of the structure closer to the bottom of the pillar. This leads to the formation of a bell-like shape, which is further enhanced by redeposition of sputtered atoms and slightly larger displacements of the outer (surface) atoms in the cascades. As the final dimensions of the SET are very restricted, the structural changes caused by the ion-beam irradiation has to be taken into consideration when aiming for a specific final geometry.

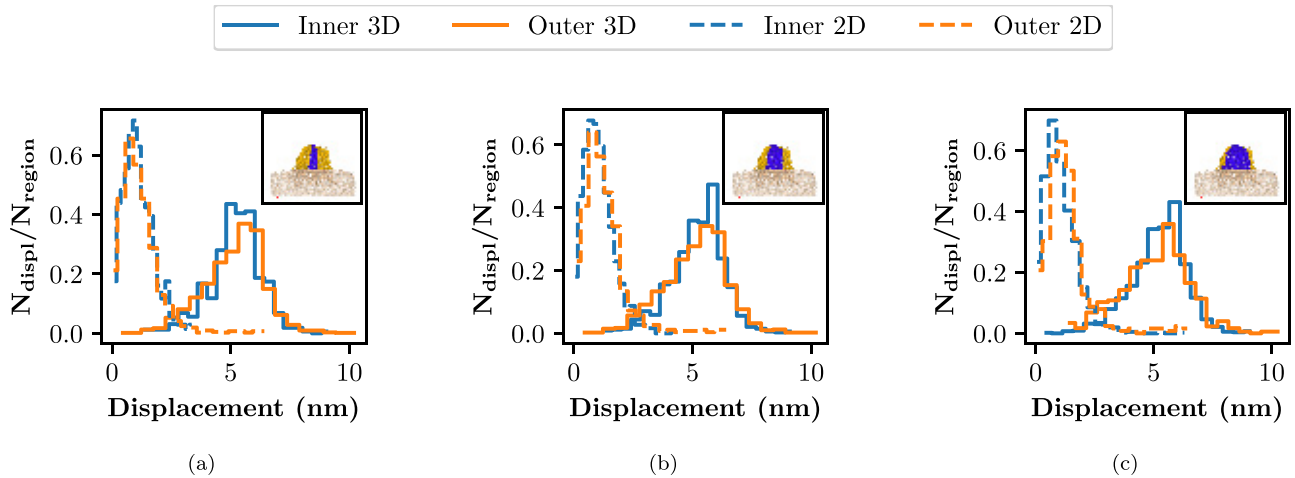


FIG. 15. Distribution of atomic displacements in the small Si nanopillar after 3000 ions. The colors separate the atoms near the surface (“outer” atoms, orange color) and close to the core of the pillar “inner” atoms, blue color). The border between inner and outer is defined at approximately (a) one quarter, (b) half, and (c) three quarters of the radius. Notations “3D” and “2D” are used to indicate total and lateral displacements, respectively. The histograms are normalized to the total amount of atoms in the dedicated region. The thickness of the outer region does not affect the displacement trend noticeably.

#### IV. CONCLUSION

When irradiating a 25 nm *c*-Si/7 nm *a*-SiO<sub>2</sub>/19 nm *c*-Si pillar with 25 keV Si<sup>+</sup> broad-beam irradiation consecutively, we observed a strong deformation of the initial structure. The deformation became stronger after the crystalline Si within the pillars rendered amorphous. The success of ion mixing was followed by increasing number of Si–Si bonds within and Si–O bonds outside the SiO<sub>x</sub> slab. However, the successful mixing was accompanied by significant shrinkage of the slab, including the diffuse borders with low concentration of O atoms. This observation indicated preferential sputtering of O atoms over Si atoms. This effect must be taken into account in the final design of the nanopillar structure to enable formation of a single QD.

The analysis of the sputtering angles indicate that redeposition of sputtered atoms might play a role in the shape modification, but is insufficient on its own to cause the major modification observed experimentally. The significant sputtering from the sides should lead to thinning of the pillar as well, but the nanopillar in the simulations did not become thinner. These observation points out the importance of the ion-hammering effect already at the nanoscale level. As a result of this effect, the nanopillar has not only shrunk in height, but also the thickness of the SiO<sub>x</sub> layer reduced visibly, and the height reduction was accompanied by a sidewise broadening of the structure. We associate the experimentally observed

bell-shape structure with the ion-hammering rather than with thermal shape smoothing at RT, i.e., the sidewise spread is caused by random walk due to ballistic collisions in cooperation with stress-relaxation effects towards open surfaces. The superlinear trend found in the total displacements along the major axis of the pillar was found to be a combination of the plastic flow in the bottom Si layer and the overall sputtering.

Revealing the behavior of the material under irradiation, we conclude that it is possible to achieve the desired atomic mixing in a buried SiO<sub>2</sub> layer with the presented pillar setup if the precaution for preferential sputtering of O atoms, in particular, at the beginning of the irradiation procedure is carefully taken into account to not negatively affect the tunneling distances of the final SET device.

#### ACKNOWLEDGMENTS

This project received funding from the European Union’s Horizon 2020 Framework Programme research and innovation program under Grant Agreement No. 688072. The views and opinions expressed herein do not necessarily reflect those of the European Commission. We thank the Finnish Grid and Cloud Infrastructure (FGCI), urn:nbn:fi:research-infras-2016072533, and CSC-IT Center for Science, Finland, for computational resources.

- [1] M. A. Kastner, *Rev. Mod. Phys.* **64**, 849 (1992).
- [2] L. Guo, *Science* **275**, 649 (1997).
- [3] Y. T. Tan, T. Kamiya, Z. A. K. Durrani, and H. Ahmed, *J. Appl. Phys.* **94**, 633 (2003).
- [4] Y. Takahashi, M. Nagase, H. Namatsu, K. Kurihara, K. Iwdate, Y. Nakajima, S. Horiguchi, K. Murase, M. Tabe, M. Nagase, K.

- Murase, S. Horiguchi, Y. Takahashi, K. Kurihara, Y. Nakajima, H. Namatsu, and M. Tabe, *Electron. Lett.* **31**, 136 (1995).
- [5] H. Ishikuro and T. Hiramoto, *Appl. Phys. Lett.* **71**, 3691 (1997).
- [6] D. V. Averin and K. K. Likharev, *J. Low Temp. Phys.* **62**, 345 (1986).

- [7] M. A. Kastner, D. Goldhaber-Gordon, H. Shtrikman, D. Mahalu, D. Abusch-Magder, and U. Meirav, *Nature (London)* **391**, 156 (1998).
- [8] S. Inaba, K. Okano, S. Matsuda, M. Fujiwara, A. Hokazono, K. Adachi, K. Ohuchi, H. Suto, H. Fukui, T. Shimizu, S. Mori, H. Oguma, A. Murakoshi, T. Itani, T. Iinuma, T. Kudo, H. Shibata, S. Taniguchi, M. Takayanagi, A. Azuma *et al.*, *IEEE Trans. Electron Devices* **49**, 2263 (2002).
- [9] C.-T. Sah, in *Proceedings of IEEE*, Vol. 76 (IEEE, New York, 1988), pp. 1280–1326.
- [10] C. P. Poole, Jr. and F. J. Owens, *Introduction to Nanotechnology* (Wiley, New York, 2003), p. 400.
- [11] D. L. Feldheim and C. D. Keating, *Chem. Soc. Rev.* **27**, 1 (1998).
- [12] B. Schmidt, K.-H. Heinig, L. Röntzsch, T. Müller, K.-H. Stegemann, and E. Votintseva, *Nucl. Instruments Methods Phys. Res. Sect. B Beam Interact. with Mater. Atoms* **242**, 146 (2006).
- [13] N. Dalosso, G. Das, S. Larcheri, G. Mariotto, G. Dalba, L. Pavesi, A. Irrera, F. Priolo, F. Iacona, and F. Rocca, *J. Appl. Phys.* **101**, 113510 (2007).
- [14] B. Liedke, K.-H. Heinig, A. Mücklich, and B. Schmidt, *Appl. Phys. Lett.* **103**, 133106 (2013).
- [15] S. Ilday, F. Ö. Ilday, R. Hübner, T. J. Prosa, I. Martin, G. Nogay, I. Kabacelik, Z. Mics, M. Bonn, D. Turchinovich, H. Toffoli, D. Toffoli, D. Friedrich, B. Schmidt, K.-H. Heinig, and R. Turan, *Nano Lett.* **16**, 1942 (2016).
- [16] X. Xu, T. Prüfer, D. Wolf, H.-J. Engelmann, L. Bischoff, R. Hübner, K.-H. Heinig, W. Möller, S. Facsko, J. von Borany, and G. Hlawacek, *Beilstein J. Nanotechnol.* **9**, 2883 (2018).
- [17] T. Müller, K.-H. Heinig, and W. Möller, *Appl. Phys. Lett.* **81**, 3049 (2002).
- [18] T. Müller, K.-H. Heinig, and W. Möller, *Mater. Sci. Eng. B* **101**, 49 (2003).
- [19] T. Müller, K.-H. Heinig, W. Möller, C. Bonafos, H. Coffin, N. Cherkashin, G. B. Assayag, S. Schamm, G. Zanchi, A. Claverie, M. Tencé, and C. Colliex, *Appl. Phys. Lett.* **85**, 2373 (2004).
- [20] E. Amat, J. Bausells, and F. Perez-Murano, *IEEE Trans. Electron Devices* **64**, 5172 (2017).
- [21] P. W. Voorhees, *J. Stat. Phys.* **38**, 231 (1985).
- [22] G. Madras and B. J. McCoy, *J. Chem. Phys.* **117**, 8042 (2002).
- [23] M.-L. Pourteau, A. Gharbi, P. Brianceau, J.-A. Dallery, F. Laulagnet, G. Rademaker, R. Tiron, H.-J. Engelmann, J. von Borany, K.-H. Heinig, M. Rommel, and L. Baier, *Micro Nano Eng.* **9**, 100074 (2020).
- [24] C. Y. Ng, T. P. Chen, and A. Du, *Phys. Status Solidi* **203**, 1291 (2006).
- [25] Ions4SET Project, <https://cordis.europa.eu/project/id/688072>.
- [26] K. Nordlund, M. Ghaly, R. S. Averback, M. Caturla, T. Diaz de la Rubia, and J. Tarus, *Phys. Rev. B* **57**, 7556 (1998).
- [27] K. Nordlund, J. Keinonen, M. Ghaly, and R. S. Averback, *Nature (London)* **398**, 49 (1999).
- [28] T. Watanabe, H. Fujiwara, H. Noguchi, T. Hoshino, and I. Ohdomari, *Jpn. J. Appl. Phys.* **38**, L366 (1999).
- [29] T. Watanabe, D. Yamasaki, K. Tatsumura, and I. Ohdomari, *Appl. Surf. Sci.* **234**, 207 (2004).
- [30] J. Samela, K. Nordlund, V. N. Popok, and E. E. B. Campbell, *Phys. Rev. B* **77**, 075309 (2008).
- [31] J. Ziegler, see <http://www.srim.org>.
- [32] C. Fridlund, J. Laakso, K. Nordlund, and F. Djurabekova, *Nucl. Instruments Methods Phys. Res. Sect. B Beam Interact. with Mater. Atoms* **409**, 14 (2017).
- [33] H. J. C. Berendsen, J. P. M. Postma, W. F. van Gunsteren, A. DiNola, and J. R. Haak, *J. Chem. Phys.* **81**, 3684 (1984).
- [34] A. Stukowski, *Model. Simul. Mater. Sci. Eng.* **18**, 015012 (2010).
- [35] X. Xu, K.-H. Heinig, W. Möller, H.-J. Engelmann, N. Klingner, A. Gharbi, R. Tiron, J. von Borany, and G. Hlawacek, *Semicond. Sci. Technol.* **35**, 015021 (2020).
- [36] G. Greaves, J. A. Hinks, P. Busby, N. J. Mellors, A. Ilinov, A. Kuronen, K. Nordlund, and S. E. Donnelly, *Phys. Rev. Lett.* **111**, 065504 (2013).
- [37] T. Mizutani, *Jpn. J. Appl. Phys.* **30**, L628 (1991).
- [38] F. Djurabekova and K. Nordlund, *Phys. Rev. B* **77**, 115325 (2008).
- [39] S. Klaumünzer and G. Schumacher, *Phys. Rev. Lett.* **51**, 1987 (1983).
- [40] A. Hedler, S. L. Klaumünzer, and W. Wesch, *Nat. Mater.* **3**, 804 (2004).
- [41] E. Snoeks, A. Polman, and C. A. Volkert, *Appl. Phys. Lett.* **65**, 2487 (1994).
- [42] A. Johannes, S. Noack, W. Wesch, M. Glaser, A. Lugstein, and C. Ronning, *Nano Lett.* **15**, 3800 (2015).
- [43] T. Diaz de la Rubia, R. S. Averback, R. Benedek, and W. E. King, *Phys. Rev. Lett.* **59**, 1930 (1987).
- [44] A. Einstein, in *Investigations on the Theory of the Brownian Movement*, edited by R. Fürth (Methuen & Company Limited, London, 1956), p. 124.
- [45] A. Lopez-Cazalilla, F. Djurabekova, A. Ilinov, C. Fridlund, and K. Nordlund, *Mater. Res. Lett.* **8**, 110 (2020).
- [46] H. Holland-Moritz, A. Ilinov, F. Djurabekova, K. Nordlund, and C. Ronning, *New J. Phys.* **19**, 013023 (2017).
- [47] K. Nordlund, F. Djurabekova, and G. Hobler, *Phys. Rev. B* **94**, 214109 (2016).
- [48] See Supplemental Material at <http://link.aps.org/supplemental/10.1103/PhysRevMaterials.5.083606> for the shape evolution of the nanopillar under irradiation.